









# Effective secondary electron yields for different surface materials in capacitively coupled plasmas

Florian Beckfeld<sup>1,\*</sup> , Ranna Masheyeva<sup>2,3</sup> , Aranka Derzsi<sup>2</sup> ,  
David A Schulenberg<sup>1,†</sup> , Ihor Korolov<sup>1</sup> , Claudia Bock<sup>4</sup> , Julian Schulze<sup>1</sup>   
and Zoltán Donkó<sup>2</sup> 

<sup>1</sup> Chair of Applied Electrodynamics and Plasma Technology, Department of Electrical Engineering and Information Science, Ruhr University Bochum, D-44780 Bochum, Germany

<sup>2</sup> Institute for Solid State Physics and Optics, HUN-REN Wigner Research Centre for Physics, 1121 Budapest, Konkoly-Thege Miklós str. 29-33, Hungary

<sup>3</sup> Department of General Physics, Satbayev University, 050013 Almaty, Kazakhstan

<sup>4</sup> Chair of Microsystems Technology, Department of Electrical Engineering and Information Science, Ruhr University Bochum, D-44780 Bochum, Germany

E-mail: [beckfeld@aept.rub.de](mailto:beckfeld@aept.rub.de)

Received 4 October 2024, revised 17 January 2025

Accepted for publication 20 February 2025

Published 14 March 2025



## Abstract

Processes at the plasma boundaries, including the electrodes, can significantly influence plasma properties, among them the plasma density, the flux-energy distribution of various particle species, etc. The emission of secondary electrons, in particular, can lead to ionization avalanches, which strongly increase the plasma density and change the discharge operation mode as a function of the operating conditions. Using reliable values to characterize the efficiency of such processes is indispensable for accurate numerical modeling. There is, however, a lack of such data for surface coefficients for arbitrary combinations of the plasma species and electrode materials and surface conditions. In this work, we investigate the  $\alpha$ - to  $\gamma$ -mode transition induced by changes of the operating conditions (voltage, pressure) in capacitively coupled argon plasmas for different electrode surface materials (copper, nickel, gold, aluminum, and stainless steel) and target the determination of the effective *in-situ* secondary electron emission coefficient,  $\gamma^*$ . The first is accomplished by phase-resolved optical emission spectroscopy applied to measure the spatio-temporal distribution of the electron-impact excitation rate from the ground state into a high-threshold-energy level of a tracer gas (neon). The studies are conducted for pressures between 50 Pa and 200 Pa and voltage amplitudes ranging from 150 V to 350 V at a driving frequency of 13.56 MHz. A transition from the  $\alpha$ - to the  $\gamma$ -mode is shown to take place at different pressures for different materials. The combination of these measurements with particle-in-cell / Monte Carlo collisions simulations employing a range of  $\gamma^*$  values allows the determination of the effective ‘*in-situ*’ electron yield for the given set of operating conditions. The simulations also shed light on the

\* Author to whom any correspondence should be addressed.

† Deceased.



Original Content from this work may be used under the terms of the [Creative Commons Attribution 4.0 licence](https://creativecommons.org/licenses/by/4.0/). Any further distribution of this work must maintain attribution to the author(s) and the title of the work, journal citation and DOI.

contributions of the various species, argon ions, metastable atoms, and vacuum-ultraviolet photons to electron emission from the electrodes. The findings suggest that for precise modeling individual secondary electron yields specific to different electrode surface materials should be used and multiple species should be included in the models that describe secondary electron emission at the electrodes.

**Keywords:** capacitively coupled plasmas, plasma surface interactions, secondary electron emission, phase-resolved optical emission spectroscopy

## 1. Introduction

Low-temperature capacitively coupled plasmas (CCPs) are used in many processing steps for the manufacturing of micro-electronic devices, for example, to etch trenches with high aspect ratios, the deposition of thin films or ion implantation, as well as the manufacturing of flat panel displays and thin film solar cells [1–3]. These discharges are favored for different aspects, e.g. the possibility to produce radicals at room temperature through electron-impact dissociation, as well as allowing the bombardment of surfaces with high energy ions, enabling to anisotropically etch a surface.

In the manufacturing of state-of-the-art semiconductor devices, where feature sizes approach a few nanometers, understanding the fundamental mechanisms that determine key plasma parameters such as particle densities and energy distribution functions is of crucial importance, in order to precisely control a process [4, 5]. These characteristics of the plasma depend on many input parameters, for example, the amplitude, frequency and shape of the driving voltage waveform, the pressure of the gas, or the gas mixture [6–10]. Ions, fast neutrals, and other species can induce the emission of secondary electrons, called  $\gamma$ -electrons, from the boundary surfaces, and at sufficient pressure and/or sheath voltage, these electrons cause ionization avalanches inside the plasma sheath, which increases the plasma density [11–14]. At gas pressures, where the mean free path becomes comparable to the dimensions of typical discharge chambers, highly energetic  $\gamma$ -electrons can collide with other surfaces leading to the emission of electron-induced secondary electrons, so-called  $\delta$ -electrons, which are a main cause of ionization in this pressure regime [15–17]. The influence of plasma-surface interactions on the plasma has been investigated in various studies [18–20], which show that both the ion flux and the ion energy at the electrodes of a CCP depend on the emission of  $\gamma$ -electrons. As a model for the emission of ion-induced secondary electrons, simulations often include a constant probability of emission,  $\gamma$  (for example  $\gamma = 0.1$ ). Material-specific data is typically determined through particle beam experiments for well-defined surface conditions [21–25], and more sophisticated models incorporate these data in their simulations [13, 18, 26]. However, it is unclear if these results can directly be transferred to plasmas, because of the poorly defined and often unknown electrode surface conditions, which can be strongly affected by the plasma through etching and deposition processes. Additionally, there is little data for such surface

coefficients at ion energies below 100 eV, which often occur in CCPs and where ion-induced secondary electrons are predominantly generated by Auger emission [18, 27]. Most importantly, in plasmas, there is a superposition of multiple mechanisms that can cause the emission of  $\gamma$ -electrons.

There are not many works that determine  $\gamma$ -coefficients under plasma conditions [20, 28–33]. Therefore, in this work, the effects of various electrode surface materials (copper, nickel, gold, aluminum, and stainless steel) on the electron power absorption and excitation dynamics are explored in a geometrically symmetric CCP reactor operated in argon (with 10% neon admixture) at pressures between 50 Pa and 200 Pa, at 13.56 MHz driving frequency, at voltage amplitudes ranging from 150 V to 350 V, and an electrode gap of 4 cm with the aim to determine the effective secondary electron emission coefficient as a function of the electrode material and the actual plasma operating conditions. Aluminum, stainless steel, and copper are chosen as they are commonly present at electrodes or walls of plasma reactors, while nickel and gold are used as hard-mask materials for plasma etching. The spatio-temporal electron-impact excitation dynamics are investigated by phase-resolved optical emission spectroscopy (PROES). Through a combination of PROES measurements and kinetic simulations, the unknown secondary electron yields of the different electrode materials are determined by two methods:

- A computationally assisted spectroscopic technique, the  $\gamma$ -CAST method [33], as a function of voltage and pressure. This method requires the plasma to be in a transition between the  $\alpha$ - and the  $\gamma$ -mode, which, as mentioned above, needs sufficient pressure or voltage, therefore the named parameter range is chosen. High pressures are favored over high voltages, as high voltages lead to the plasma igniting in the chamber's side flanges, disturbing the symmetry of the system.
- A pixel-based comparison of the measured and computationally generated images of the distributions of the electron-impact excitation rate. This method has the advantage that it operates as well when the discharge is outside the transition between the  $\alpha$ - and the  $\gamma$ -mode.

We find that the  $\alpha$ - to  $\gamma$ -mode transition occurs at a different pressure depending on the surface material, indicating that each material has a distinct secondary electron yield.

Additionally, the comparison of the experimental and the computational results reveals that the effective secondary electron yield,  $\gamma^*$ , which is affected by contributions from positive ions, metastable atoms, and vacuum-ultraviolet photons, decreases as a function of voltage because of the varying fluxes of these species as a function of the operating conditions. These findings demonstrate the importance of including surface material-specific  $\gamma$ -coefficients into simulations.

The paper is structured as follows: section 2 describes the experimental setup and the simulation method. In sections 3 and 4, details on the calculation of the effective secondary electron yield are given, while the results are presented and discussed in section 5. Finally, in section 6, conclusions are drawn.

## 2. Methods

### 2.1. Experimental setup

To investigate the effect of the boundary surface on a low temperature plasma, electrodes made of different materials are placed inside a geometrically symmetric CCP reactor. This reactor (figure 1) consists of two plane parallel electrodes with equal surface areas inside a cylinder made of borosilicate glass [34]. The advantage of the geometrically symmetric plasma source is that it allows comparison with one-dimensional simulations, such as the ones that are used in this study. A detailed description of the setup can be found in [35].

Our experiments are conducted using argon with an admixture (10%) of neon as a tracer gas [36]. The gases are supplied into the chamber through two mass flow controllers (MFCs, Type 1179B, MKS and F-200CV, Bronkhorst). The vacuum inside the chamber is created by a system of pumps consisting of a rotary vane pump (Trivac D2.5E, Oerlikon Pfeiffer Vacuum) and a turbomolecular pump (Turbovac SL 80, Oerlikon Pfeiffer Vacuum).

The plasma is created by a radio frequency (RF) power generator (Cesar 136, Advanced Energy), which delivers a sinusoidal voltage waveform at 13.56 MHz. The power is coupled to the plasma via an impedance matching network (VarioMatch 1000, Advanced Energy). The voltage drop across the plasma is measured by a voltage probe (PHVS662-L, PMK) and an oscilloscope (Waverunner LT364, LeCroy). The voltage is measured at the top lid of the reactor chamber. Previous works have shown that the voltage drop between the top lid and the top electrode is negligible [35].

To investigate the spatio-temporal emission of the plasma using the method of phase-resolved optical emission spectroscopy (PROES), an ICCD camera (intensified charge-coupled device, 4picos, Stanford Computer Optics) is used. The camera is triggered by a synchronization signal provided by the RF generator. The trigger signal is shifted in time by a delay generator (DG353, Stanford Research Systems). In this way, by measuring the emission of the plasma within a time window of 1 ns and shifting the trigger signal by the same time, the emission is measured time-resolved over one RF period. By

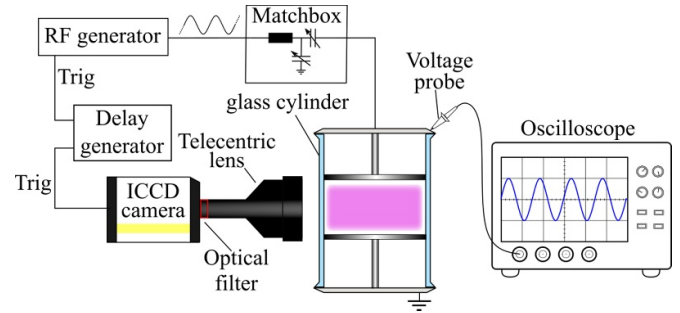


**Figure 1.** Schematic of the experimental setup, containing the geometrically symmetric reactor chamber, the camera system consisting of an ICCD camera and a delay generator, the electrical system consisting of the RF generator and a matchbox as well as a voltage probe and an oscilloscope.

applying a rate equation model, the electron-impact excitation from the ground state into a specifically chosen highly excited level can be calculated from the measurement of the emission [36]. A telecentric lens (MVTC23013, Thorlabs) ensures that only parallel light rays enter the camera, resulting in a constant optical resolution along the line of sight. An optical bandpass filter (585.5NB3, Omega Optical) allows measuring the emission that results from the Ne  $2p_1$  level at 585.25 nm [37]. Based on the rate equation model [36], the electron-impact excitation rate from the neon ground state into the Ne  $2p_1$  level is then determined.

Five different surface materials are used in this study. For three materials, stainless steel, aluminum, and copper, the whole electrodes are made of the named material. The other materials, nickel and gold, are thin films with a thickness of approximately 100 nm that are deposited on a silicon wafer by e-beam evaporation. In this form, these materials are used as etching masks in plasma processing. For better adhesion to the silicon surface, a thin layer of chromium (10 nm) is deposited underneath the gold layer. These silicon wafers with the etching masks are then glued on top of stainless steel electrodes with conductive vacuum epoxy (H21D, Epoxy Technology). The surfaces are not sputter cleaned, therefore they should generally be categorized as ‘dirty’ surfaces according to the terminology introduced in [23]. The PROES measurements are performed for  $L = 4$  cm electrode gap, at pressures between  $p = 50$  Pa and 200 Pa, and voltage amplitudes of  $U = 150$  V, 250 V, and 350 V.

### 2.2. Simulation method

In our work, we use a hybrid simulation framework, as described by Donkó *et al* [38], for an accurate description of the Ar CCP. This framework consists of an extended electrostatic PIC/MCC simulation module and a Diffusion–Reaction–Radiation (DRR) module. These two modules are executed iteratively during the course of the simulation. The model considers a one-dimensional scenario. The particle-in-cell / Monte Carlo collisions (PIC/MCC) and the DRR modules, as well as their interfacing, have been described in detail

in a previous work [38], which was aimed at the investigation of Ar metastable atom kinetics [39] in a CCP. Thus, here only a concise summary of the approach is given.

In the 1d3v PIC/MCC module, besides ground-state Ar atoms, populations of Ar atoms in 30 excited levels are also considered as targets for electron-impact collisions. The ground-state atoms are assumed to be distributed homogeneously (according to the gas pressure and temperature, which are taken from the experiments at  $p \leq 100$  Pa [35] and using extrapolated values at higher pressures). The density distributions of the excited atoms are derived in the DRR module (see later).

Electron collisions with ground-state Ar atoms include elastic scattering, excitation to 30 specific Ar-I levels and to a lumped ‘Rydberg’ level, as well as ionization. Electron collisions with Ar atoms in excited levels include stepwise excitation, superelastic collisions, and stepwise ionization. The cross sections of these processes are taken from the BSR database [40, 41] of LXCat [42, 43], except for the stepwise ionization for which the source of data is the work by Hyman [44]. Here, in order to increase the computational speed, some of the low-rate stepwise excitation and superelastic collision processes are neglected. These low-rate processes are selected (as in Masheyeva *et al* [45]) based on prior computations using the full set of processes [38]. For the  $\text{Ar}^+$  ions, the collision model is based on Phelps and Petrovic [23], with cross sections for backscattering and isotropic (elastic) scattering channels.

Principal discharge characteristics (i.e. the electric potential and the charged particle densities) are computed at the points of an equidistant grid, with  $\Delta x$  resolution. Poisson’s equation is solved for the electric potential considering the electrode potentials as boundary conditions and the space charge created by the charged particles. Time is discretized to units of  $\Delta t$  and the positions and the velocities of the charged particles, i.e. electrons and  $\text{Ar}^+$  ions, respectively, are advanced with  $\Delta t_e = \Delta t$  and  $\Delta t_i = 20\Delta t$ . Collisions are treated with a standard Monte Carlo method [46, 47]. The simulations are carried out for the same discharge conditions, as used in the experiments, with  $f = 13.56$  MHz excitation frequency and  $L = 4$  cm electrode gap, and discharge voltage amplitudes of  $U = 150$  V, 250 V, and 350 V. In the simulations, the pressure is set equal to the partial pressure of argon in the gas mixture, i.e. to 90% of the total gas pressure. As Ne atoms have significantly higher excitation and ionization threshold energies as compared to Ar atoms, under the conditions of this study only marginal excitation/ionization of Ne atoms occur. Thus, it is expected that the presence of the Ne admixture has only a very limited effect on the plasma properties and the electron energy distribution function in the CCP under investigation here, i.e. simulating a pure Ar plasma is justified.

The excitation period  $T = 1/f$  is divided into  $N_t = 5000 \dots 16000$  time steps depending on the gas pressure, in order to keep the collision probability of the charged species during one time step at a low value.  $N_g = 1600$  grid points are used for all parameter combinations to resolve the Debye length. These simulation settings respect the stability and accuracy criteria of the PIC/MCC scheme (see, e.g. [48,

49]). The rates of all electron-impact collision processes are acquired during the course of the PIC/MCC simulation using a grid of  $N_r = 60$  points. This latter, coarse grid is used later in the DRR module to solve the particle balance equations of the excited species. As no sharp spatial variations of these species are present in our system, the use of relatively low number of grid points is sufficient and makes computations more efficient.

The interaction of the charged particles with the boundary surfaces includes (i) the neutralization of the ions and, associated with this, the emission of a secondary electron with a probability expressed by the (effective) emission yield (or secondary electron emission coefficient, SEEC)  $\gamma^*$ , and (ii) the elastic reflection of the impinging electrons, characterized by the coefficient  $r$ . While more sophisticated models for the interaction of the electrons with surfaces exist [50–52], for the conditions of the present study no inelastic reflection and emission of true ( $\delta$ ) secondary electrons is expected to play a role due to the very limited range of the energy of the electrons reaching the electrode surfaces.

The rates of the electron-impact collision processes derived in the PIC/MCC module are next fed into the DRR module. There, the densities of the excited atoms are computed by solving the diffusion equations for these species (for technical details see [38]), considering the rates obtained in the PIC/MCC module and the rates of the radiative channels (spontaneous emission and re-absorption), pooling ionization between the excited atoms, as well as the quenching of the excited levels by neutrals, and radial diffusion. The rate of the pooling ionization is adopted from Lymberopoulos and Economou [53], while the data that characterize radiative transitions (Einstein coefficients, level multiplicities) from Siepa *et al* [54, 55]. The solution also includes the effect of the quenching of the  $1s_5$  and  $1s_3$  metastable levels, taken from Tachibana [56] and the  $2p$  levels by neutrals, taken from Sadeghi *et al* and Chang *et al* [57, 58]. The diffusion coefficient of the excited species is taken from Ellis and Twiddy [59], with a temperature dependence from Chai and Kwon [60]. The trapping of the radiation, which is very strong for the resonant, but also non-negligible for some other transitions, is accounted for by an escape factor,  $\eta$ . This quantity is taken from Bhatia and Kastner [61] (using equations (6a) and (6b), which originate from Capriotti [62], however in [61] typographical errors of in the work of [62] have been corrected). After solving the diffusion equations for the Ar excited level populations, these data are fed back to the PIC/MCC module for the next iteration step. This iteration continues until a converged solution is obtained (typically after several thousand RF cycles).

The principal output of the computations is the spatio-temporal excitation rate of the Ne  $2p_1$  level which can readily be compared with the experimental data. These ‘excitation maps’ are computed for a set of discharge voltages and gas pressures, and for a sequence of secondary electron emission coefficients for any fixed pair of  $U$  and  $p$ . This procedure allows determining  $\gamma^*$  via searching for the best match between the computed and measured maps at the same



discharge conditions, using methods described in section 4. In the PIC/MCC simulation, neon is treated as a tracer gas, i.e. the excitation rate of the Ne 2p<sub>1</sub> level is computed by calculating the collision frequency of the  $e^- + \text{Ne} \rightarrow e^- + \text{Ne}$  2p<sub>1</sub> process along the trajectories of the electrons, while no actual collisions of this type take place. At LXCat [42], various databases provide (somewhat different) cross sections for this excitation process and experimental data are also available in the literature. From LXCat, we use data from the Biagi database (MAGBOLTZ versions 7.1 and 8.9) [63, 64], the BSR database [40, 41], and the Puech database [65, 66]. The experimental data sources include the works of Chilton [67] and Tsurubuchi [68]. In the PIC/MCC module, excitation maps using these cross sections are derived simultaneously. These cross sections, as will be discussed upon the presentation of the results, yield somewhat different excitation rates, presumably due to their slightly different behaviour near the energy threshold of the excitation process.

### 3. The effective secondary electron yield

It is important to note that in a low-pressure gas discharge, several types of species can contribute to charge reproduction (secondary electron emission) at the electrodes [23]. While positive ions are often considered to be the most important or even the only species that lead to secondary electron emission, contributions of metastable atoms, fast neutrals, and VUV photons to secondary electron emission were also found to be important in studies of DC (Townsend) discharges [23]. While the contributions of these species are rarely addressed in studies of RF discharges, we believe that a comprehensive model needs to include the effects of these multiple species. At some conditions (typically in high-voltage CCPs at very low pressures) electron-induced electron emission may also play a major role [15–17], this process has, however, no effect at the conditions studied here.

Considering a one-dimensional setting, the emitted flux of the secondary electrons at an electrode can be given as

$$-\Gamma_e = \gamma_i \Gamma_i + \gamma_m \Gamma_m + \gamma_a \Gamma_a + \gamma_p \Gamma_p, \quad (1)$$

where the ‘i’, ‘m’, ‘a’, and ‘p’ indexes stand for, respectively, positive ions, metastable atoms, fast neutrals, and photons, the  $\Gamma$ -s are the fluxes of the respective species, and the  $\gamma$ -s their secondary yields. An *effective secondary electron yield* can be defined as the ratio of the emitted electron flux to the incoming ion flux, i.e.

$$\gamma^* = \left| \frac{\Gamma_e}{\Gamma_i} \right| = \frac{\gamma_i \Gamma_i + \gamma_m \Gamma_m + \gamma_a \Gamma_a + \gamma_p \Gamma_p}{\Gamma_i}. \quad (2)$$

It is to be noted that in a PIC/MCC simulation where only ions are traced and therefore, only the effect of ions on secondary electron emission can be quantified, the contributions of other species (mentioned above) can also be taken into account implicitly by using an effective electron yield.

We expect that the effective electron yield,  $\gamma^*$ , changes as a function of discharge conditions ( $p$  and  $U$ ) and also depends on the electrode material. The contributions of the various species can be accounted for by considering the following arguments:

- for the positive ions, under the discharge conditions considered here, the potential electron ejection mechanism is dominant [27] as the ions arrive at the electrodes with low kinetic energies. For a given material, we do not expect that  $\gamma_i$  changes significantly due to varying  $p$  and  $U$  (in the ranges covered here);
- the yield  $\gamma_m$  that characterizes metastable atoms can be approximated to be the same as that for the positive ions (as it is the high potential energy of ions and metastables that plays the role in the ejection of electrons) [69];
- the photoelectric yield,  $\gamma_p$ , at the wavelength of the resonant lines in the  $\approx 100$  nm wavelength range varies significantly in the literature. Values of 0.05–0.15 were given in [70–72] and a significantly lower value of 0.006 was found in [23] to yield the best agreement between experimental and modeling results for argon Townsend discharges. While there is relatively large uncertainty between the data sources, we do not expect that for a given material  $\gamma_p$  depends on  $p$  and  $U$  in the present experiment;
- we do not expect fast neutrals (originating from  $\text{Ar}^+ + \text{Ar}$  collisions) in an energy range where the kinetic ejection mechanism is operational, therefore the term with  $\gamma_a$  in the above equation can be neglected.

The flux of metastable atoms, as well as the flux of the VUV radiation, can readily be obtained from the DRR part of the simulation code. With these, equation (2) for the effective electron yield simplifies to

$$\gamma^* = \gamma_i \left( 1 + \frac{\Gamma_m}{\Gamma_i} \right) + \gamma_p \frac{\Gamma_p}{\Gamma_i}. \quad (3)$$

From the comparison of the experimental and computational results for the Ne 2p<sub>1</sub> excitation maps we can derive the effective yield  $\gamma^*$ . Using the  $\Gamma_m/\Gamma_i$  and  $\Gamma_p/\Gamma_i$  ratios obtained from the calculations, equation (3) may provide a way to obtain approximate values of  $\gamma_i$  and  $\gamma_p$  which are characteristic for a given material but depend only marginally on the discharge conditions. This possibility will be explored upon the presentation of the results.

## 4. Determination of the effective secondary electron yield

### 4.1. Comparison of spatio-temporal excitation maps with $\gamma$ -CAST

The  $\gamma$ -CAST method [33], which is based on the comparison of the spatio-temporal distribution of the electron-impact excitation rate of specific atomic levels derived experimentally (by PROES measurements) and computationally (by PIC/MCC simulations) for the determination of the effective secondary electron yield of the electrode material ( $\gamma^*$ ), is

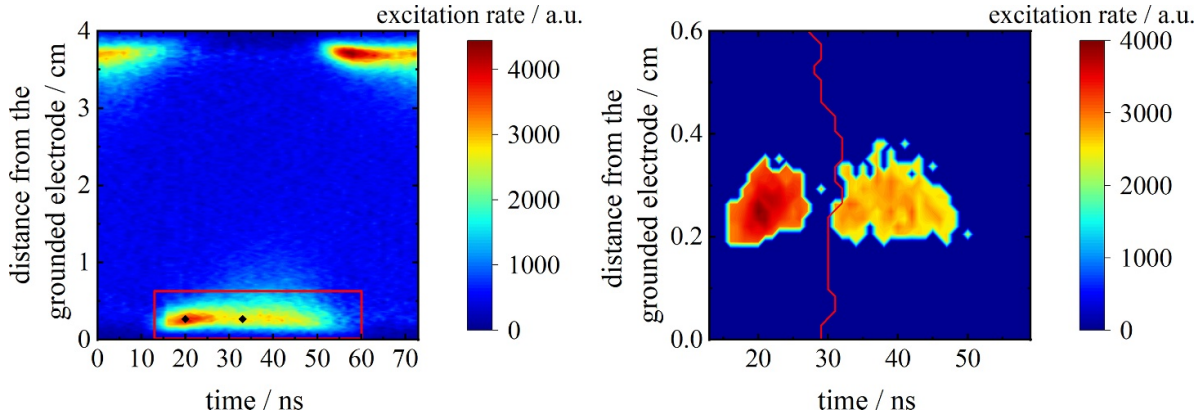


**Figure 2.** Illustration of the peak-finding and -separation by the  $\gamma$ -CAST algorithm. Left: Spatio-temporal plot of the electron impact excitation rate from the ground state to the Ne  $2p_1$  level obtained from PROES. The red rectangle marks the region of interest (ROI) and the black squares mark the detected maxima in the  $\alpha$ - and  $\gamma$ -peaks in the ROI. The horizontal axis corresponds to one RF period, and the vertical axis represents the electrode gap. Right: Isolated  $\alpha$ - and  $\gamma$ -peaks. The red line marks the line separating the peaks found by the image segmentation algorithm. Discharge conditions:  $p = 100$  Pa,  $L = 4$  cm,  $f = 13.56$  MHz,  $U = 350$  V, copper electrodes.

applied here. This method is based on determining the intensity ratio of specific regions of the spatio-temporal excitation rate, characteristic for the  $\alpha$ - and  $\gamma$ - discharge operation modes. We will apply a refined version of this method proposed by Schulenberg *et al* [73]. As the method was explained in detail in the mentioned reference, we will only give a brief description of how we applied the algorithm to our data here. The method is illustrated in figure 2 by using PROES data obtained with copper electrodes located at a distance of 4 cm, at a total (90% Ar + 10% Ne) pressure of 100 Pa, 13.56 MHz driving frequency, and 350 V voltage amplitude. The following steps are employed to calculate the intensities of the  $\alpha$ - and  $\gamma$ -peaks and their ratio:

- (i) Selection of a region of interest (ROI) in the excitation map which includes both the  $\alpha$ - and the  $\gamma$ -peak (figure 2, left, red rectangle).
- (ii) Find the maxima of the  $\alpha$ - and  $\gamma$ -peaks within this area (figure 2, left, black squares).
- (iii) Apply a watershed image segmentation algorithm [74] to the negation of the ROI to determine a border that splits the ROI into two parts, containing the  $\alpha$ - and  $\gamma$ -peak, respectively. The border determined by this algorithm is shown as a red line in the right panel of figure 2.
- (iv) In both parts of the original, non-negated ROI, remove all the data points that are below a certain threshold of a percentage of the maximum in the respective area, 85% in our case.
- (v) Average the remaining values after removal of the background in the two areas to get  $I_\alpha$  and  $I_\gamma$ , respectively, and to calculate the  $I_\gamma/I_\alpha$  ratio.

#### 4.2. Pixel-based similarity of spatio-temporal excitation map images

An alternative of the  $\gamma$ -CAST method, that also combines PROES measurements with PIC/MCC simulations for the

determination of the  $\gamma^*$  coefficient, is introduced here. In contrast to  $\gamma$ -CAST, this approach does not necessitate the simultaneous presence of both the  $\alpha$ -peak and  $\gamma$ -peak in the spatio-temporal map of the electron-impact excitation rate, making it applicable across a wider range of discharge conditions. The method relies on the similarity of images, specifically the pixel-based similarity of the maps of the spatio-temporal distribution of the electron impact excitation rate from the ground state into a specific level (Ne  $2p_1$  level in this work), obtained from measurements and simulations. The method is illustrated in figure 3 by using PROES data obtained for copper electrodes, for the same discharge conditions as in figure 2. The simulations are performed with different  $\gamma^*$  coefficients set as input values. Note the marked change of the excitation patterns with changing  $\gamma^*$  in the simulation.

For the comparison of the spatio-temporal maps of the electron impact excitation rate obtained from PROES and the simulations, the following steps are followed:

- (i) The data from PROES measurement (figure 3, first row) are initially processed to remove the background noise and the simulation data matrices are reshaped to match the size of the PROES data matrix (see the result in figure 3, second row). In the comparison, only the regions close to the grounded electrode (highlighted by dashed gray rectangles in the panels in the second row) are used.
- (ii) Grayscale images of the regions marked by the dashed gray rectangles are created (panels in the third row). In the grayscale image corresponding to the PROES data (first panel in the third row), a ‘scan area’ (shown as a red rectangle) is defined, capturing the dominant excitation pattern at the grounded electrode.
- (iii) The ‘scan area’ (image) is compared to rectangles (images) of the same size extracted from the simulation data for a given  $\gamma^*$  (panels 2–4 in the third row). The sum of squared differences (SSD), a measure of match based on pixel-by-pixel intensity differences, is calculated for all possible image pairs. This involves the summation of

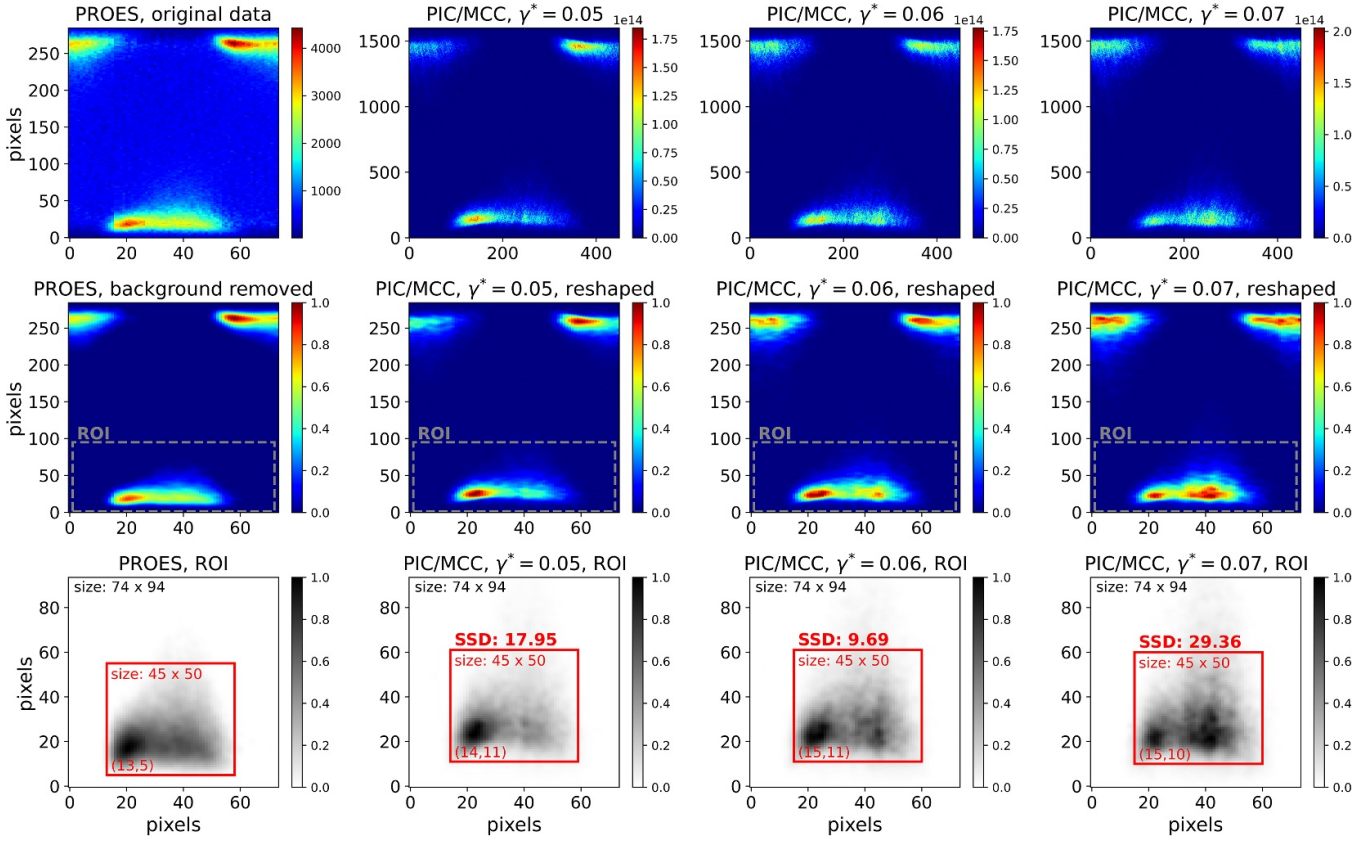


**Figure 3.** Illustration of the pixel-based comparison of excitation rate maps from PROES and PIC/MCC. First row: Spatio-temporal plots of the electron impact excitation rate from the ground state into the Ne 2p<sub>1</sub> level obtained by PROES and from PIC/MCC simulations for different values of the effective secondary electron yield. Second row: Data from PROES measurements initially processed to remove the background noise alongside simulation data matrices reshaped to match the size of the PROES data matrix. Last row: Grayscale plots of the regions considered for pixel-based comparison. The red rectangles indicate the ‘scan area’ defined in the PROES image, along with corresponding regions of the same size in the PIC/MCC images where the best match (i.e. minimum SSD value) was obtained for the different  $\gamma$  coefficients. The SSD values for these cases are shown in the panels. The plots in the second and the third rows are individually normalized to a maximum of 1. Discharge conditions:  $p = 100$  Pa,  $L = 4$  cm,  $f = 13.56$  MHz,  $U = 350$  V, copper electrodes.

squares for the product of pixel subtraction between the two images.

- (iv) The above steps are performed repeatedly for all simulations with different  $\gamma^*$  coefficients (see the minimum SSD values obtained for different  $\gamma$  in panels 2–4 in the second third row).
- (v) The best match between PROES and PIC/MCC results is indicated by the minimum of all SSD values. The  $\gamma$ -coefficient used in the simulation for which the minimum SSD value was obtained in the comparison, is considered the effective secondary electron yield of the electrode surface material,  $\gamma^*$ .

For the exemplary case presented in figure 3,  $\gamma = 0.06$  results in the best agreement between PROES and PIC/MCC data. In order to eliminate slight shifts in time and space between the experimental and computed images, a shift is allowed along both  $x$  and  $t$  during the fitting process.

From the two methods presented above, only the first has been used previously in similar studies [33, 75]. One reason for using a new method here as well is that a relatively good agreement between the data derived based on the completely

different approaches gives assurance for the reliability of the results. Moreover, while the first method is operational only in cases when clear  $\alpha$ - and  $\gamma$ -peaks can be identified in the spatio-temporal excitation maps, the second method also allows the derivation of the ‘matching’ effective secondary electric yield in cases where either of the peaks is missing as no separation of the two peaks is required. Differences between the values for the apparent electron yield derived via both methods—none of them being perfect when used with real, noisy data—provide information about the accuracy of the results.

## 5. Results

### 5.1. Comparison of surface materials

To investigate the effects of different surface materials on the electron power absorption and excitation dynamics, PROES measurements are performed for copper, nickel, gold, aluminum, and stainless steel electrode surfaces. In the experiments, the same material is used for both electrodes. PROES measurements are done by varying the pressure and the voltage amplitude to monitor transitions from the  $\alpha$ - to the  $\gamma$ -mode



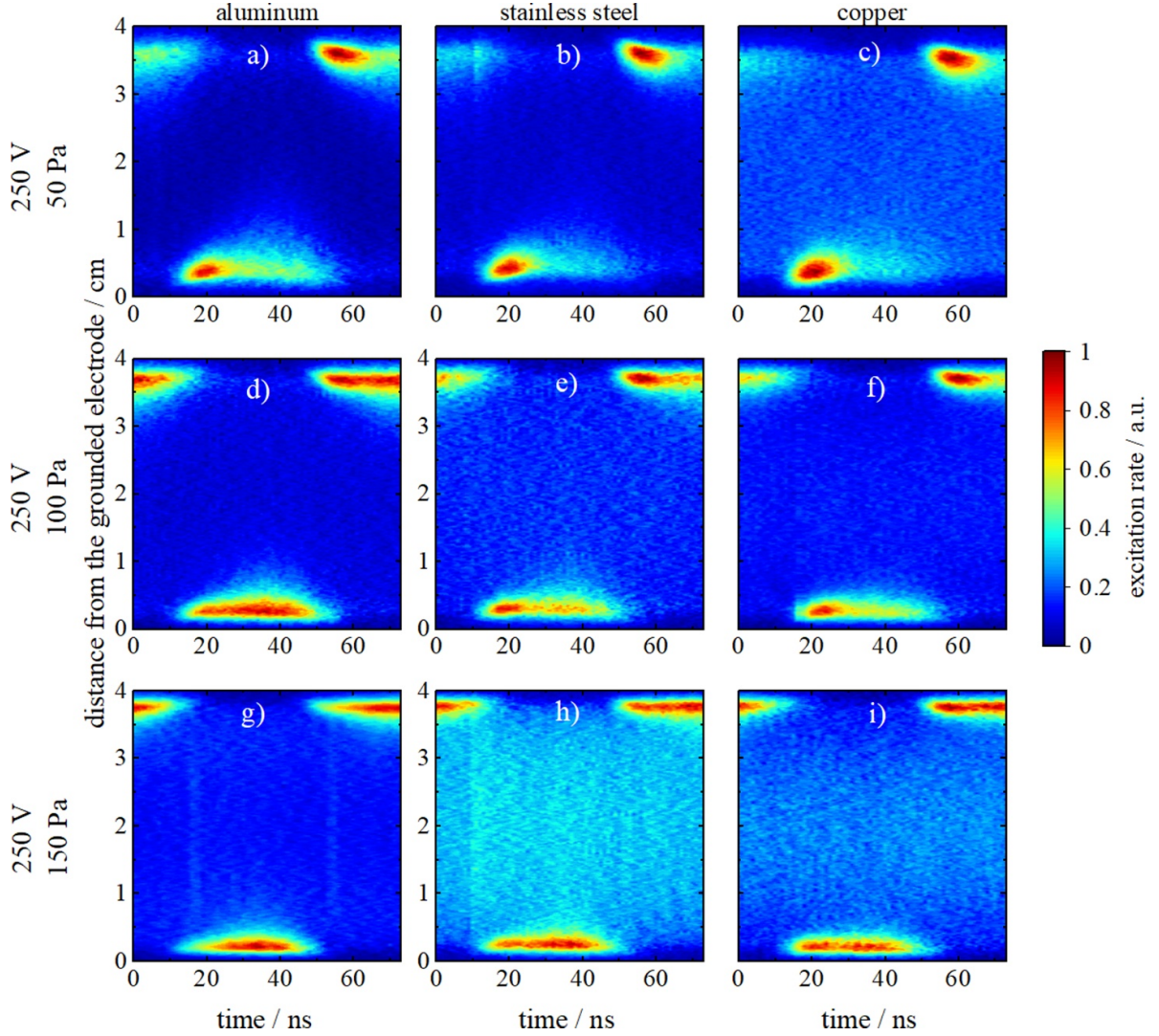


**Figure 4.** Spatio-temporal plots of the electron-impact excitation rate from the ground state to the Ne  $2p_1$  level measured with PROES for different electrode materials: aluminum (first column), stainless steel (second column) and copper (third column) at 50 Pa (first row), 100 Pa (second row) and 150 Pa (third row), respectively. Each plot is normalized to its maximum. Discharge conditions:  $L = 4$  cm,  $f = 13.56$  MHz,  $U = 250$  V.

[11]. In figure 4, the spatio-temporal electron-impact excitation rates from the ground state to the Ne  $2p_1$  level obtained from PROES measurements with aluminum, stainless steel and copper electrodes at different pressures are shown. On the abscissa of each plot, one whole RF period (74 ns) is shown, while the ordinate shows the distance from the grounded electrode. Each plot is normalized to its maximum, hence the absolute rate of excitation cannot be compared between two pairs of plots. The amplitude of the applied voltage amplitude is 250 V in all measurements shown and the pressure is 50 Pa, 100 Pa and 150 Pa, respectively.

For the measurements done at 50 Pa (figures 4(a)–(c)), one can see strong excitation at the expanding sheath edges at both electrodes at  $t \approx 20$  ns and  $t \approx 60$  ns (dominant  $\alpha$ -peak), which indicates discharge operation in the  $\alpha$ -mode for all materials. In the measurement with aluminum, however, excitation inside the sheath regions is also substantial at both electrodes at the times around the local full sheath expansion ( $t \approx 0$  ns and

$t \approx 35$  ns), i.e. the  $\gamma$ -peak becomes slightly visible in contrast to the other two materials. By increasing the pressure to 100 Pa (figures 4(d)–(f)), the electron power absorption mode shifts from the dominant  $\alpha$ -mode at 50 Pa to the hybrid  $\alpha/\gamma$ -mode, which means that both the  $\alpha$ - and  $\gamma$ -peaks are present for all materials. However, a difference in the ratio of the respective peaks is obtained for the different electrode materials: while the electron power absorption mode is quite similar for all three materials at 50 Pa, one can see that at 100 Pa, the  $\gamma$ -peak dominates over the  $\alpha$ -peak for aluminum, while for stainless steel and copper it is vice versa, the  $\alpha$ -peak is stronger than the  $\gamma$ -peak. When comparing stainless steel and copper, the  $\gamma$ -peak of stainless steel appears to be slightly stronger. At the highest pressure of 150 Pa (figures 4(g)–(i)) the  $\gamma$ -peak is enhanced for all materials. The measurement with the aluminum electrode shows the plasma to be completely in the  $\gamma$ -mode, as there is no  $\alpha$ -peak, but only the strong  $\gamma$ -peak is present. For stainless steel and copper electrodes, the hybrid



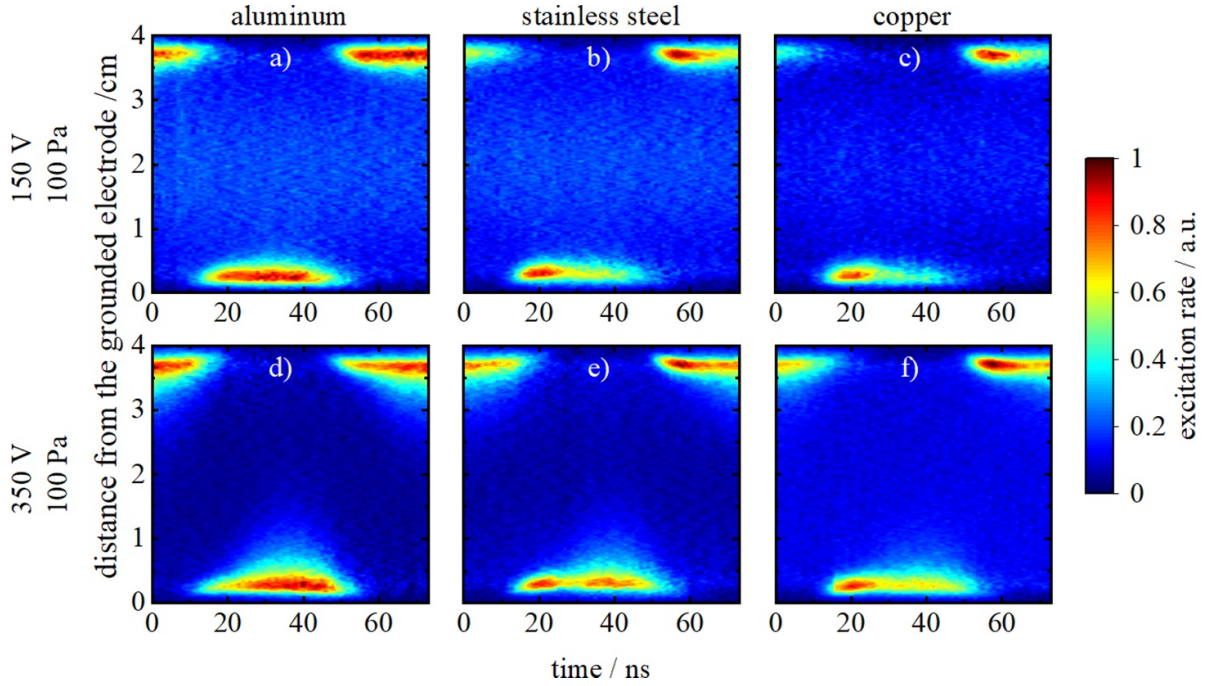


**Figure 5.** Spatio-temporal plots of the electron-impact excitation rate from the ground state to the Ne  $2p_1$  level measured with PROES for different electrode materials: aluminum (first column), stainless steel (second column) and copper (third column) at 150 V (first row) and 350 V (second row), respectively. Each plot is normalized to its maximum. Discharge conditions:  $L = 4$  cm,  $f = 13.56$  MHz,  $p = 100$  Pa.

$\alpha/\gamma$ -mode is observed. However, when comparing the intensity of the  $\alpha$ - and  $\gamma$ -peak to each other in both measurements, the  $\gamma$ -peak dominates over the  $\alpha$ -peak for stainless steel, while both peaks are similarly strong for copper. At all pressures presented in figure 4, the  $\gamma$ -peak is the strongest in the measurements with the aluminum electrodes, the weakest  $\gamma$ -peak is obtained for the copper electrodes, and results for stainless steel are between the two.

Figure 5 shows the spatio-temporal electron-impact excitation rate from the ground state into the Ne  $2p_1$  level, for aluminum, stainless steel, and copper at a pressure of 100 Pa and voltages of 150 V (top row) and 350 V (bottom row). At a voltage of 150 V (figures 5(a)–(c)), the measurement with aluminum electrodes shows a dominant  $\gamma$ -peak, while for stainless steel and copper the  $\alpha$ -peak is dominant. When the voltage is set to 350 V, the discharge is in the  $\gamma$ -mode in the presence of aluminum electrodes, while the intensities of the  $\alpha$ - and  $\gamma$ -peaks are equally strong in the presence of the stainless steel and for copper electrodes, the  $\alpha$ -peak dominates over the  $\gamma$ -peak.

As observed from the results of the pressure variation, for a variation of the voltage, it is also seen that the  $\gamma$ -peak is most dominant in the presence of aluminum electrodes and the least dominant for copper electrodes. As the intensity of the  $\gamma$ -peak is determined by the efficiency of secondary electron emission at the electrodes, these measurement results suggest that these materials have a different  $\gamma^*$ -coefficient, with the relation  $\gamma_{Al}^* > \gamma_{SS}^* > \gamma_{Cu}^*$ , where  $\gamma_{Al}^*$ ,  $\gamma_{SS}^*$  and  $\gamma_{Cu}^*$  correspond to the effective secondary electron yields of aluminum, stainless steel, and copper surfaces, respectively.

## 5.2. Determination of $\gamma$ -coefficients

The PROES measurements discussed in the previous section show that, at the same external parameters (pressure, voltage), the intensity ratio of the  $\gamma$ - and  $\alpha$ -peaks is different for each electrode material. In the following, the unknown  $\gamma$ -coefficients of the different materials are determined using the  $\gamma$ -CAST method.

In this work, we want to compare the measured excitation rate of the Ne  $2p_1$  level directly to the corresponding excitation rate obtained from the simulation. This comes with the challenge of properly selecting the cross section for this process to be used in the simulations. In the LXCat database for cross section sets, there are multiple data sets for the Ne  $2p_1$  excitation to choose from, additional data sets are also available in the literature (as already mentioned in section 2.2).

To illustrate the effects of the choice of the excitation cross section for the Ne  $2p_1$  level, figure 6 shows excitation maps obtained from simulations with some of the different cross sections (listed in section 2.2) and  $\gamma^* = 0.07$ ,  $U = 250$  V and  $p = 150$  Pa. The data reveal that significant differences occur in these maps depending on the choice of the cross section for the Ne  $2p_1$  excitation process. This implies that great care must be taken when cross sections are selected for any modeling work, as all cross sections used here originate from reliable sources: either from LXCat or from publications in prestigious journals. We chose the cross section given in [67] for the further analysis as this cross section originates from well-documented experimental studies and a tabulated form of the data was available.

In the left column of figure 7, the  $I_\gamma/I_\alpha$  peak intensity ratios as a function of voltage at different pressures, for different

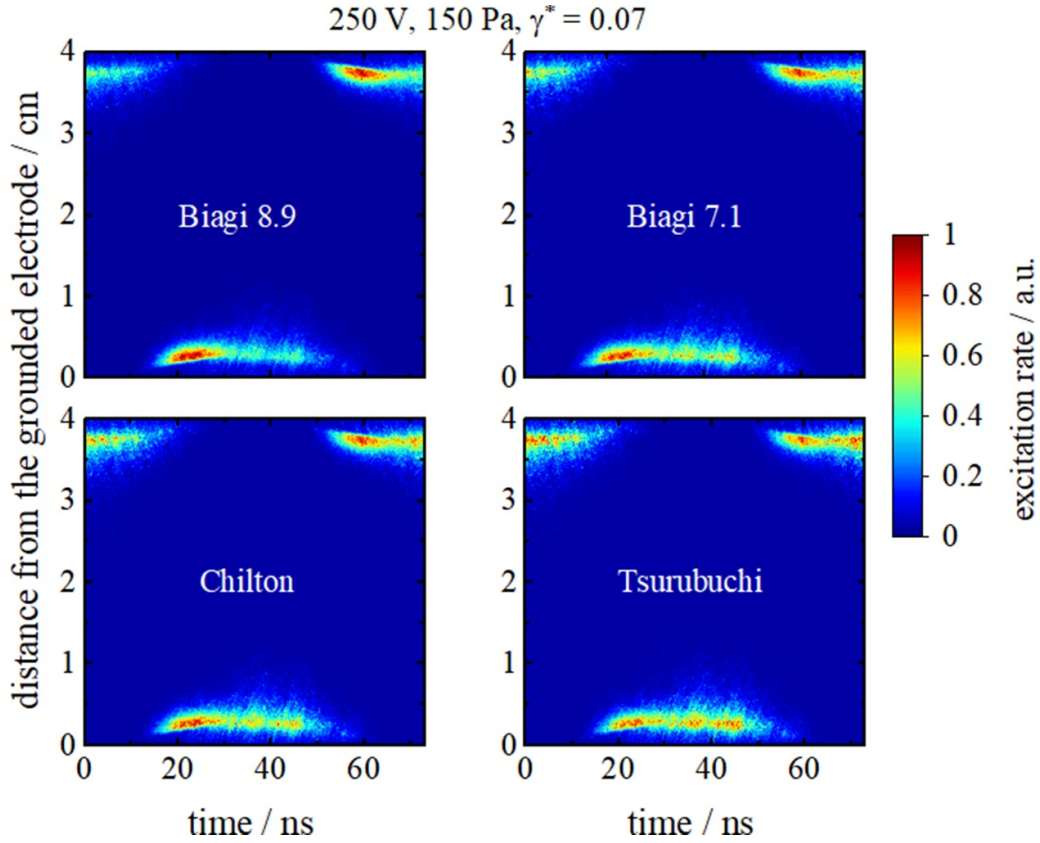


**Figure 6.** Spatio-temporal plots of the electron-impact excitation rate from the ground state into the Ne  $2p_1$  level obtained from PIC/MCC simulations at the same voltage amplitude  $U = 250$  V, pressure  $p = 150$  Pa, and  $\gamma^* = 0.07$  with different Ne  $2p_1$  cross section sets from the Biagi database (MAGBOLTZ versions 7.1 and 8.9) [63, 64] obtained from LXCat, as well as experimentally determined cross sections from Chilton [67] and Tsurubuchi [68].

electrode materials (copper, nickel, gold, aluminum and stainless steel) are shown. Please note that these ratios could only be determined for measurements where both the  $\alpha$ - and  $\gamma$ -peaks were present in the excitation map, therefore the  $I_\gamma/I_\alpha$ -ratio cannot be calculated for every voltage-pressure combination covered in this study. Furthermore, the parameter range in which data points are available is different for the different electrode materials as the intensity of the  $\gamma$ -peak is material dependent, e.g. for materials with a high  $\gamma^*$  only the  $\gamma$ -peak is present at high pressures, while the  $\alpha$ -peak is still visible for materials with low  $\gamma^*$ . Additionally to the  $I_\gamma/I_\alpha$  ratios, the middle column of figure 7 shows the values of the effective secondary electron yield  $\gamma^*$ , which resulted in the best agreement obtained from the measurement and the simulations based on comparing the peak intensity ratio and the right column shows the values obtained for  $\gamma^*$  based on pixel-based similarity. The results for copper electrodes (figure 7, top row) show that  $\gamma^*$  decreases as a function of the voltage amplitude from 0.12 at 150 V to 0.06 at 350 V.

The observed change in  $\gamma^*$  as a function of voltage can be explained by the variation of the ratio of the ion flux  $\Gamma_i$ , the metastable flux  $\Gamma_m$ , and the (VUV) photon flux  $\Gamma_p$  at the electrodes at different voltages. Figure 8 shows the relative photon flux with respect to the ion flux  $\Gamma_p/\Gamma_i$  on the left axis and the metastable flux with respect to the ion flux and  $\Gamma_m/\Gamma_i$  on the right axis, respectively, as a function of voltage, obtained

from the simulations for copper electrodes. The photon flux decreases relative to the ion flux when the voltage increases. The relative flux of metastables and ions,  $\Gamma_m/\Gamma_i$ , is also decreasing with increasing voltage, similar to the relative flux of  $\Gamma_p/\Gamma_i$ . Even though the absolute change in flux ratio is smaller for  $\Gamma_m/\Gamma_i$  than for  $\Gamma_p/\Gamma_i$ , the decrease of  $\Gamma_m/\Gamma_i$  still is expected to have an impact on  $\gamma^*$ , as  $\gamma_m \gg \gamma_p$  can be assumed based on the findings of Phelps and Petrovic [23] and Molnar [69], which were described section 3. Considering these findings in equation (3), the second and third terms containing the secondary electron emission by metastables and photons, respectively, get smaller at higher voltages, resulting in  $\gamma^*$  decreasing with voltage.

The dependence of the flux ratios,  $\Gamma_m/\Gamma_i$  and  $\Gamma_p/\Gamma_i$ , on the discharge voltage is a consequence of the change of the rates of the main excitation and ionization pathways, being the electron impact excitation and ionization of ground-state atoms. Computing this ratio,  $R$ , by dividing the spatially and temporally averaged total electron-impact excitation rate of ground state atoms with the spatially and temporally averaged electron-impact ionization rate of ground state atoms, we obtain  $R = 2.35$  for 150 V voltage amplitude,  $R = 1.74$  for 250 V, and  $R = 1.41$  for 350 V. This change shows that with increasing voltage ionization becomes the more preferred process for electron-impact collisions as compared to excitation. This is a result of the specific energy-dependence of the

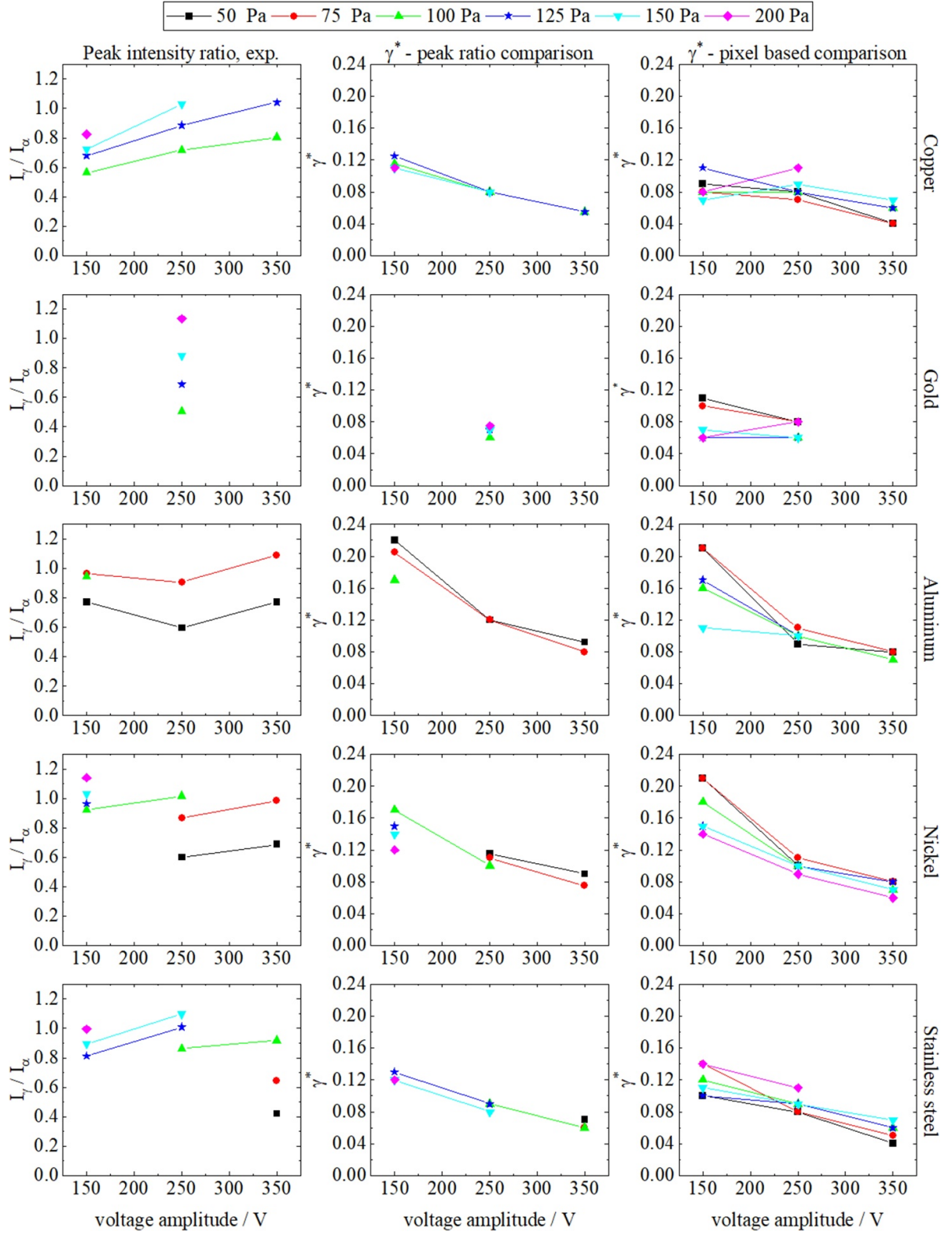


**Figure 7.** Determination of  $\gamma^*$  for the materials used in this study. Left column:  $I_\gamma/I_\alpha$  peak intensity ratios obtained from the experiments. Middle column:  $\gamma^*$  values for the simulations that matched the experiments best based on comparing the peak intensity ratios. Right column:  $\gamma^*$  values for the simulations that matched the experiments best based on the pixel-based comparison.



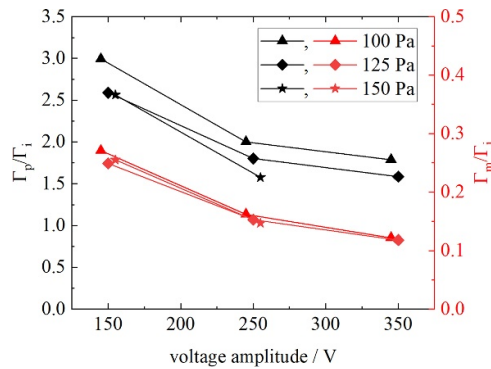


**Figure 8.** Ratio of metastable flux to ion flux,  $\Gamma_m/\Gamma_i$  (right axis), and ratio of photon flux to ion flux,  $\Gamma_p/\Gamma_i$  (left axis), at the electrode surfaces obtained from simulations with the respective  $\gamma^*$  that corresponds to the measurements with copper electrodes. Points are slightly offset horizontally for better readability.

cross sections of the respective processes and the changes of the Electron Energy Distribution Function.

The trends found for the behavior of the effective yield,  $\gamma^*$ , for copper surfaces at different pressures and voltages can be observed for all materials except gold. In the case of gold surfaces, the  $\gamma$ -peak was not visible at 150 V and measurements could not be done at 350 V due to deposition of the material on the walls of the reactor. While for copper and stainless steel, the slope in  $\gamma^*$  is constant when increasing the voltage amplitude, for nickel and aluminum the slope of  $\gamma^*$  is steeper between 150 V and 250 V than between 250 V and 350 V. This may be due to the removal of surface layers of oxide by the plasma, leading to an increase in  $\gamma^*$ .

Besides the  $\gamma$ -CAST method (based on a comparison of the peak intensity ratios), the effective secondary electron yield for the different electrode materials is also determined by using a pixel-based comparison of the excitation maps (see section 4). The application of the second method serves to validate the results obtained from the  $\gamma$ -CAST method and is shown in the right column of figure 7. A comparison of the results of the two methods shows similar trends in the outcomes of the method relying on pixel-based comparison as it was observed before by using the  $\gamma$ -CAST method: the effective secondary electron emission yield  $\gamma^*$  increases with decreasing the voltage. Furthermore, the comparison of the whole excitation matrices in the second method rather than just comparing the peak intensity ratios in the  $\gamma$ -CAST, allows to determine the effective yield,  $\gamma^*$ , also in cases where only the  $\alpha$ - or the  $\gamma$ -peak is present in the excitation maps. This provides additional valuable information on the effective yields under discharge conditions where the  $\gamma$ -CAST-method is not applicable. For example in the measurements where the electrode surfaces were made of gold and the  $\gamma$ -peak was only visible for voltage amplitudes of 250 V, the trend that the  $\gamma^*$  increases with decreasing voltage amplitude still holds true.

From the point where it has been shown that the particle fluxes of different species to the electrode impact  $\gamma^*$ , it may seem consequential to use equation (3) to determine  $\gamma_i$  and  $\gamma_p$  from the data. Our analysis, of which the details are not shown

here, however, indicates that this is an ‘ill-posed’ problem, a set of possible combinations of  $\gamma_i$  and  $\gamma_p$  result in approximately the same  $\gamma^*$  that was determined by the simulations. Therefore, the present diagnostic technique appears to be limited to the determination of  $\gamma^*$ .

## 6. Conclusion

In this work, the effects of different electrode surface materials on the electron power absorption and excitation dynamics have been investigated in a geometrically symmetric CCP operated in argon. PROES measurements have been performed for various electrode materials (copper, nickel, gold, aluminum, and stainless steel), for a gap length of 4 cm, for 13.56 MHz, pressures between 50 Pa and 200 Pa, and voltage amplitudes between 150 V and 350 V. Combining PROES measurements and simulations, the effective, *in-situ* secondary electron yields of the different electrode materials have been determined by the  $\gamma$ -CAST method.

It was found that, at a constant voltage amplitude, the pressure where the discharge transitions from the  $\alpha$ - to the  $\gamma$ -mode is different for each material. Additionally, it has been found that this  $\gamma^*$  depends on the amplitude of the applied voltage, as the atomic levels that produce VUV photons get populated less effectively at higher voltage amplitudes and therefore the removal of electrons from the electrode surface gets less effective, which leads to a decrease in  $\gamma^*$ . Because there has been no thorough cleaning of oxidized layers or other structures forming on the electrode surface, all materials can be categorized as ‘dirty’ surfaces. In [23] it is stated that all dirty materials have approximately the same  $\gamma$ -coefficient, which does not match with our results.

As the  $\gamma$ -coefficient influences both the ion flux and ion energy at the electrodes, the presented work shows that for precise modeling, a surface-material specific  $\gamma$ -coefficient should be included in simulations.









## Data availability statement

The data that support the findings of this study are available at <https://rdpcidat.rub.de/node/1151>.

## Acknowledgments

This work was supported by the German Research Foundation in the frame of projects 138690629 (C1 and T09) and 428942393 and by the Federal Ministry of Education and Research in the frame of the ForMikro project FlexTMDSense (Grant Number 16ES1096K). RM, AD, and ZD have been supported by the Hungarian Office for Research, Development, and Innovation (NKFIH) via the Grant K134462. AD received support from the J Bolyai Scholarship of the Hungarian Academy of Sciences (HAS). The authors thank Professor C C Lin for sharing the tables of Ne excitation cross sections from [67].

## ORCID iDs

Florian Beckfeld  <https://orcid.org/0000-0001-8605-2634>  
 Ranna Masheyeva  <https://orcid.org/0000-0002-6950-662X>  
 Aranka Derzsi  <https://orcid.org/0000-0002-8005-5348>  
 David A Schulenberg  <https://orcid.org/0000-0002-4086-8678>  
 Ihor Korolov  <https://orcid.org/0000-0003-2384-1243>  
 Claudia Bock  <https://orcid.org/0000-0003-0933-9556>  
 Julian Schulze  <https://orcid.org/0000-0001-7929-5734>  
 Zoltán Donkó  <https://orcid.org/0000-0003-1369-6150>

## References

- [1] Chabert P and Braithwaite N 2011 *Physics of Radio-Frequency Plasmas* (Cambridge University Press)
- [2] Lieberman M A and Lichtenberg A J 2005 *Principles of Plasma Discharges and Materials Processing* (Wiley)
- [3] Donnelly V M and Kornblit A 2013 *J. Vac. Sci. Technol. A* **31** 050825
- [4] Adamovich I et al 2022 *J. Phys. D: Appl. Phys.* **55** 373001
- [5] Faraz T, Verstappen Y G, Verheijen M A, Chittok N J, Lopez J E, Heijdra E, van Gennip W J, Kessels W M M and Mackus A J 2020 *J. Appl. Phys.* **128** 213301
- [6] O'Neill J A and Singh J 1995 *J. Appl. Phys.* **77** 497–504
- [7] Baek K H, Lee E, Klick M and Rothe R 2017 *J. Vac. Sci. Technol. A* **35** 021304
- [8] Bojarov A, Radmilovic-Radjenovic M and Savic M 2010 *Publ. Astron. Obs. Belgrade* **65** 1–8
- [9] Derzsi A, Korolov I, Schüngel E, Donkó Z and Schulze J 2013 *Plasma Sources Sci. Technol.* **22** 065009
- [10] Krüger F, Wilczek S, Mussenbrock T and Schulze J 2019 *Plasma Sources Sci. Technol.* **28** 075017
- [11] Belenguer P and Boeuf J P 1990 *Phys. Rev. A* **41** 4447–59
- [12] Donkó Z, Schulze J, Hartmann P, Korolov I, Czarnetzki U and Schüngel E 2010 *Appl. Phys. Lett.* **97** 081501
- [13] Daksha M, Derzsi A, Wilczek S, Trieschmann J, Mussenbrock T, Awakowicz P, Donkó Z and Schulze J 2017 *Plasma Sources Sci. Technol.* **26** 085006
- [14] Schulze J, Donkó Z, Schüngel E and Czarnetzki U 2011 *Plasma Sources Sci. Technol.* **20** 045007
- [15] Hartmann P et al 2021 *J. Phys. D: Appl. Phys.* **54** 255202
- [16] Horváth B, Daksha M, Korolov I, Derzsi A and Schulze J 2017 *Plasma Sources Sci. Technol.* **26** 124001
- [17] Sun J Y, Wen D Q, Zhang Q Z, Liu Y X and Wang Y N 2019 *Phys. Plasmas* **26** 063505
- [18] Daksha M, Derzsi A, Mujahid Z, Schulenberg D, Berger B, Donkó Z and Schulze J 2019 *Plasma Sources Sci. Technol.* **28** 034002
- [19] Wen Y Y, Zhang Y R, Jiang G, Song Y H and Wang Y N 2019 *AIP Adv.* **9** 055019
- [20] Wen D Q, Krek J, Gudmundsson J T, Kawamura E, Lieberman M A, Zhang P and Verboncoeur J P 2023 *Plasma Sources Sci. Technol.* **32** 064001
- [21] Hagstrum H D 1956 *Phys. Rev.* **96** 325–35
- [22] Jacobsson H and Holmén G 1994 *Phys. Rev. B* **49** 1789–95
- [23] Phelps A V and Petrovic Z L 1999 *Plasma Sources Sci. Technol.* **8** R21–R44
- [24] Buschhaus R, Prenzel M and von Keudell A 2022 *Plasma Sources Sci. Technol.* **31** 025017
- [25] Kim H K, Kim T S, Lee J and Jo S K 2007 *Phys. Rev. B* **76** 165434
- [26] Derzsi A, Korolov I, Schüngel E, Donkó Z and Schulze J 2015 *Plasma Sources Sci. Technol.* **24** 034002
- [27] Hagstrum H D 1954 *Phys. Rev.* **96** 336
- [28] Depla D, Li X Y, Mahieu S and Gryse R D 2008 *J. Phys. D: Appl. Phys.* **41** 202003
- [29] Qin S, Bradley M P, Kellerman P L and Saadatmand K 2002 *Rev. Sci. Instrum.* **73** 1153–6
- [30] Sobolewski M A 2021 *Plasma Sources Sci. Technol.* **30** 025004
- [31] Sobolewski M A 2024 *Plasma Sources Sci. Technol.* **33** 085011
- [32] Schulze C, Donkó Z and Benedikt J 2022 *Plasma Sources Sci. Technol.* **31** 105017
- [33] Daksha M, Berger B, Schuengel E, Koepke M, Schulze J, Korolov I, Derzsi A and Donko Z 2016 *J. Phys. D: Appl. Phys.* **49** 234001
- [34] Godyak V A, Piejak R B and Alexandrovich B M 1990 *Rev. Sci. Instrum.* **61** 2401–6
- [35] Schulenberg D A, Korolov I, Donkó Z, Derzsi A and Schulze J 2021 *Plasma Sources Sci. Technol.* **30** 105003
- [36] Schulze J, Schüngel E, Donkó Z, Luggenhölscher D and Czarnetzki U 2010 *J. Phys. D: Appl. Phys.* **43** 124016
- [37] Kramida A, Ralchenko Y and Reader J (NIST ASD Team) 2022 NIST Atomic Spectra Database (ver. 5.10) National Institute of Standards and Technology, Gaithersburg, MD (available at: <https://physics.nist.gov/asd>) (Accessed 4 January 2023)
- [38] Donkó Z, Hartmann P, Korolov I, Schulenberg D, Rohr S, Rauf S and Schulze J 2023 *Plasma Sources Sci. Technol.* **32** 065002
- [39] Makabe T 2019 *J. Phys. D: Appl. Phys.* **52** 213002
- [40] BSR database (available at: [www.lxcat.net](http://www.lxcat.net)) (Accessed 5 September 2023)
- [41] Zatsarinny O 2006 *Comput. Phys. Commun.* **174** 273–356
- [42] Pitchford L C et al 2017 *Plasma Process. Polym.* **14** 1600098
- [43] Carbone E, Graef W, Hagelaar G, Boer D, Hopkins M M, Stephens J C, Yee B T, Pancheshnyi S, van Dijk J and Pitchford L 2021 *Atoms* **9** 16
- [44] Hyman H 1979 *Phys. Rev. A* **20** 855
- [45] Masheyeva R, Hartmann P, Luo L Y, Dzhumagulova K, Liu Y X, Schulze J and Donkó Z 2025 *J. Phys. D: Appl. Phys.* **58** 045208
- [46] Birdsall C K 1991 *IEEE Trans. Plasma Sci.* **19** 65–85
- [47] Verboncoeur J P 2005 *Plasma Phys. Control. Fusion* **47** A231–60
- [48] Lymberopoulos D P and Economou D J 1995 *J. Res. Natl. Inst. Stand. Technol.* **100** 473–94
- [49] Kim H, Iza F, Yang S, Radmilović-Radjenović M and Lee J 2005 *J. Phys. D: Appl. Phys.* **38** R283
- [50] Braginsky O, Kovalev A, Lopaev D, Proshina O, Rakhimova T, Vasilieva A, Voloshin D and Zyryanov S 2011 *J. Phys. D: Appl. Phys.* **45** 015201
- [51] Hannesdottir H and Gudmundsson J 2016 *Plasma Sources Sci. Technol.* **25** 055002
- [52] Derzsi A, Horváth B, Donkó Z and Schulze J 2020 *Plasma Sources Sci. Technol.* **29** 074001
- [53] Lymberopoulos D P and Economou D J 1993 *J. Appl. Phys.* **73** 3668–79
- [54] Siepa S, Danko S, Tsankov Ts V, Mussenbrock T and Czarnetzki U 2014 *J. Phys. D: Appl. Phys.* **47** 445201
- [55] Siepa S L 2017 Global collisional-radiative model for optical emission spectroscopy of argon and argon-containing plasmas *PhD Thesis Dissertation* Ruhr-Universität Bochum, Bochum
- [56] Tachibana K 1986 *Phys. Rev. A* **34** 1007
- [57] Sadeghi N, Setser D, Francis A, Czarnetzki U and Döbele H 2001 *J. Chem. Phys.* **115** 3144–54
- [58] Chang R and Setser D 1978 *J. Chem. Phys.* **69** 3885–97
- [59] Ellis E and Twiddy N 1969 *J. Phys. B: At. Mol. Phys.* **2** 1366
- [60] Chai K B and Kwon D H 2019 *J. Quant. Spectrosc. Radiat. Transfer* **227** 136–44

- [61] Bhatia A and Kastner S 2000 *J. Quant. Spectrosc. Radiat. Transfer* **67** 55–63
- [62] Capriotti E R 1965 *Astrophys. J.* **142** 1101
- [63] Biagi MAGBOLTZ 7.1 database (available at: [www.lxcat.net](http://www.lxcat.net)) (Accessed 5 September 2023)
- [64] Biagi MAGBOLTZ 8.9 database (available at: [www.lxcat.net](http://www.lxcat.net)) (Accessed 5 September 2023)
- [65] LxCat Puech database (available at: [www.lxcat.net/Puech](http://www.lxcat.net/Puech)) (Accessed 5 September 2023)
- [66] Puech V and Mizzi S 1991 *J. Phys. D: Appl. Phys.* **24** 1974
- [67] Chilton J E, Stewart J M and Lin C C 2000 *Phys. Rev. A* **61** 052708
- [68] Tsurubuchi S, Arakawa K, Kinokuni S and Motohashi K 2000 *J. Phys. B: At. Mol. Opt. Phys.* **33** 3713
- [69] Molnar J 1951 *Phys. Rev.* **83** 940
- [70] Feuerbacher B and Fitton B 1972 *J. Appl. Phys.* **43** 1563–72
- [71] Cairns R B and Samson J A R 1966 *J. Opt. Soc. Am.* **56** 1568
- [72] Laulainen J, Kalvas T, Koivisto H, Komppula J and Tarvainen O 2015 *AIP Conf. Proc.* **1655** 020007
- [73] Schulenberg D A, Vass M, Klich M, Donkó Z, Klotz J, Bibinov N, Mussenbrock T and Schulze J 2024 *Plasma Chem. Plasma Process.* **44** 1217–35
- [74] Bertrand G 2005 *J. Math. Imaging Vis.* **22** 217–30
- [75] Horváth B, Derzsi A, Schulze J, Korolov I, Hartmann P and Donkó Z 2020 *Plasma Sources Sci. Technol.* **29** 055002